

Original scientific paper

THE EFFECT OF ELECTRON-BEAM TREATMENT ON THE DEFORMATION BEHAVIOR OF THE EBAM Ti-6Al-4V UNDER SCRATCHING

Artur R. Shugurov, Anton Y. Nikonov, Andrey I. Dmitriev

Institute of Strength Physics and Materials Science SB RAS, Tomsk, Russia

Abstract. *The effect of the continuous electron beam scanning (CEBS) post-treatment on the microstructure, mechanical properties and scratching behavior of the Ti-6Al-4V alloy samples produced by electron beam additive manufacturing was studied experimentally and by using molecular dynamics simulation. It was found that the CEBS post-treatment resulted in the transformation of the microstructure of the samples from the α' -martensite into the $\alpha+\beta$ structure. The evolution of the sample microstructure was shown to provide improved mechanical characteristics as well as enhanced deformation recovery after scratching. A mechanism was proposed based on the results of molecular dynamics simulation, which attributed the improved recovery of the scratch grooves after passing the indenter to reversible $\beta \rightarrow \alpha \rightarrow \beta$ phase transformations, which occurred in the vanadium alloyed Ti crystallites.*

Key Words: *Ti-6Al-4V Alloy, Electron Beam Additive Manufacturing, Scratch Testing, Molecular Dynamics, Microstructure, Phase Transformations*

1. INTRODUCTION

Titanium alloys are among the most extensively used structural materials, especially in aerospace and biomedical applications [1]. This is due to the beneficial mechanical properties of titanium and its alloys, namely its high specific strength and excellent fatigue resistance, as well as biocompatibility and corrosion resistance. Dual phase titanium alloys composed of HCP- α phase and BCC- β phase, particularly Ti-6Al-4V, which alone occupies about half of the global titanium product market, are the most popular titanium alloys.

One of the main drawbacks of the titanium alloys is their poor machinability, which results in a large amount of material waste and significantly increases the cost of manufacturing titanium components from the mill products [2]. Therefore, in recent years, additive manufacturing (AM) also termed 3D printing, which provides for the building of

Received November 10, 2021 / Accepted January 08, 2022

Corresponding author: Andrey I. Dmitriev

Institute of Strength Physics and Materials Science SB RAS, 634055, pr. Akademicheski 2/4 Tomsk, Russia

E-mail: dmitr@ispms.ru

net shape structures of complex geometry by layer-by-layer adding of a material, has been considered the most promising technology for producing titanium components [3-6]. However, high temperature gradients and a rapid solidification of the molten material lead to the formation of metastable phases in the additively manufactured $\alpha+\beta$ titanium alloys. In particular, the presence of martensitic α' -phase is usually observed in as-built AM Ti-6Al-4V samples [7-9]. Although such microstructure is characterized by high strength (>1000 MPa), it suffers from poor ductility and low toughness [4, 10, 11]. Therefore, post-manufacturing heat treatments are generally required to transform the unfavorable α' -microstructure into equilibrium $\alpha+\beta$ structure [12-14].

A large variety of heat-treatment routes have been proposed to improve the microstructure and mechanical properties of AM Ti-6Al-4V [5, 15-18]. However, these processes require additional equipment that inevitably increases the manufacturing costs. In contrast, the electron beam post-treatment, which is widely used for surface finishing, modification and alloying of metals, can be performed directly in an electron beam additive manufacturing (EBAM) machine. This technology involves two different approaches: (i) applying of defocused high-current pulsed electron beams (HCPEB) to the large surface area [19-21] and (ii) continuous electron beam scanning (CEBS) of the sample surface with a focused electron beam [22-24]. Usually both the methods use rather powerful electron beams that results in melting the surface layer of a material followed by its rapid cooling and solidification. The latter, as in the case of the additive manufacturing, favors the formation of metastable microstructures [20, 22]. However, at lower energy inputs the electron beam irradiation can be used for heat treatment of AM components after their production. The CEBS process appears to be more suitable for this aim because it provides more homogeneous heating of a sample as well as lower heating and cooling rates compared with the HCPEB process.

In this study the continuous electron beam scanning was used for post-treatment of as-built EBAM Ti-6Al-4V samples in order to investigate its effect on the microstructure and mechanical properties of the dual phase titanium alloy. Scratch testing of the as-built and CEBS treated samples was performed to study their ploughing and recovery behavior. Scratch testing has been shown to be an adequate method for investigating plastic deformation of metals. It was used to study the effect of crystallographic orientations of grains [25, 26], internal interfaces [27, 28], different phases and inclusions [26, 29] on their plastic behavior of materials. This technique also proved its capability to reveal the development of strain-induced phase transformations [30, 31]. The molecular dynamics (MD) simulation of the mechanical behavior of materials subjected to scratch testing has been successfully used for investigating defect nucleation as well as development of plastic deformation. Defect-free single crystals with FCC [32-34] and BCC [35-37] crystal lattice as well as HCP crystals have been in the focus of the MD simulations. Therefore, the experimental results obtained in the present work are supported by molecular dynamic simulation of scratching the α - and β -Ti single crystals, which revealed the mechanisms of the formation of structural defects and phase transformations in the contact zone between the indenter and crystal.

2. EXPERIMENTAL DETAILS

Two rectangular Ti-6Al-4V bars with dimensions of 25 mm \times 25 mm \times 70 mm (length \times width \times height) were obtained by wire-feed electron beam additive manufacturing using an EBM machine 6E400. Grade 5 titanium wire 1.6 mm in diameter was used as a feed

material. The chemical composition of the wire corresponds to ASTM B348-13 [38]. An electron gun with a plasma cathode operated at an accelerating voltage of 30 kV was used to melt the wire. The distance between the source of the electron beam and the baseplate with dimensions of 150 mm × 150 mm × 10 mm was 630 mm. The angle between the baseplate and wire feed was 35°. The feed rate was 2 m/min. 22 layers were formed, each 3.2 mm thick. The first three layers were formed at a beam current of 24 mA followed by its decreasing to 21 mA. The 3D-printing strategy of the samples consisted in travelling the baseplate relative to the electron beam along a meander trajectory with mirror fused layers with a speed of 4 mm/s. The distance between the adjacent tracks within the same layer was ~ 3 mm. After welding each layer the baseplate went down by 3 mm.

After cooling to room temperature, one of the bars was subjected to electron beam treatment in the EBM machine. The treatment consisted in continuous scanning the bar with an elliptically shaped beam spot (the major axis, which was perpendicular to the scanning direction, was 27 mm long, the minor axis was ~0.5 mm) moving along the bar with a speed of 10 mm/s. The accelerating voltage and beam current were 30 kV and 10 mA, respectively. During the treatment the bar was heated up to a temperature of 1040 °C and held at this temperature for 5 min followed by its cooling in vacuum to room temperature. The bars were separated from the baseplate and cut along the growth direction into 2 mm thick plates using spark cutting. The rectangular samples 10×10 mm in size and 2 mm thick were cut from the plates.

The microstructure of the as-built and CEBS treated EBAM Ti-6Al-4V samples was investigated using an Axiovert 40 Mat optical microscope (Carl Zeiss, Göttingen, Germany). The samples for the examination were subjected to mechanical grinding and polishing followed by etching with Kroll's reagent. The phase composition of the samples was studied using X-ray diffraction (XRD) with a Shimadzu XRD-7000 X-ray diffractometer (Shimadzu Corporation, Kyoto, Japan). The XRD-experiments were performed in the Bragg-Brentano geometry using CuK α radiation ($\lambda = 1.5406 \text{ \AA}$). The measurements of the mechanical properties of the samples as well as their scratch testing were carried out using a NanoTest system (Micro Materials Ltd., Wrexham, UK). The nanoindentation was performed in a load controlled mode with a Berkovich diamond tip at a maximum load of 50 mN. Hardness H and Young's modulus E were determined using the Oliver-Pharr method [39].

The scratch tests were performed using a conical diamond with an apex angle of 120° and a tip curvature radius of 25 μm . The scratching was carried out with a constant velocity of 10 $\mu\text{m/s}$. 400 μm long scratching tracks were applied to all samples. The scratching process consisted of three steps. Initially surface profiles of the tested samples were scanned (step 1) with a load of 0.1 μN (no wear occurs at this load). During scratching (step 2), the surface profile could be sensed and recorded by the depth sensing system. After scratching, the surface profiles of the samples along the scratch lines were scanned again (step 3) to record the deformation recovery. In the second step, the normal load applied to the indenter was linearly ramped between 0 and 200 μm scratching to a maximum load of 200 mN, while between 200 and 400 μm the load was constant at 200 mN. 5 scratches were performed for each sample. The surface topography of the samples in the vicinity of the scratch tracks was scanned using a Solver HV atomic force microscope (AFM, NT-MDT Co., Moscow, Russia) operating in a contact mode. A series of 10 cross-sectional profiles of the scratch tracks were made and averaged to determine the residual scratch depth for each titanium sample.

3. MODEL DESCRIPTION

In order to elucidate the experimentally observed phenomena of deformation of titanium samples with different crystallographic structures, two initially defect-free titanium crystallites were considered. Crystallite 1 corresponded to the α -phase of pure Ti, while crystallite 2 represented the β -phase of Ti–6Al–4V alloy as shown in Fig. 1. Each simulated crystallite had a shape of parallelepiped with dimensions of $30.0 \times 26.0 \times 12.5$ nm along the X , Y and Z directions, respectively. The total number of atoms in both cases exceeded half of one million. Taking into account the experimental data, the spatial orientation of the elementary crystal lattice in the laboratory coordinate system for the crystallite 1 was chosen as $[\bar{1}6\bar{5}0]$, $[52\bar{3}7]$, $[\bar{3}12\bar{2}]$, along the X , Y and Z axes, correspondingly. In the case of crystallite 2, the $[100]$, $[010]$ and $[001]$ directions of the BCC crystal lattice were oriented along the X , Y and Z axes, respectively. Crystallite 2 contained 13 at. % of vanadium that corresponded to a content of 4 wt. % in the model sample, which is typical for Ti–6Al–4V alloy.

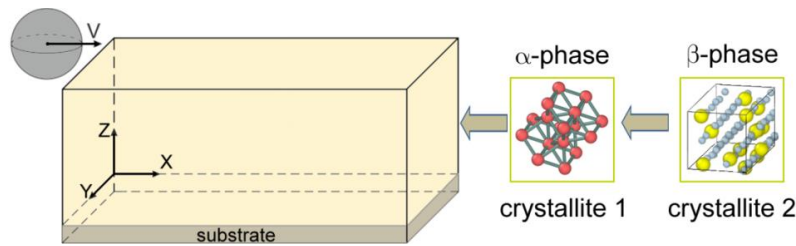


Fig. 1 MD model of the scratch test for Ti crystallites with α -phase (HCP) and β -phase (BCC) structures

Scratching of the samples was realized through the movement of an indenter along the X axis at a fixed depth of 3.5 nm with a constant scratching speed of 15 m/s. The indenter has a spherical shape with a radius R of 6.5 nm. Thus, atoms, which distance from the center of the indenter r was less than equilibrium radius R , were acted upon by a force directed from the force center and equal to

$$F = -k(R - r)^2, \quad (1)$$

where k is the tip stiffness coefficient. In our calculations, coefficient k was chosen to be equal to $0.1 \text{ eV}/\text{\AA}^3$ similar to the earlier works [25, 28, 40]. A 1.5 nm thick bottom layer (shown grey in Fig. 1) simulated a fixed substrate, while the other surfaces of the sample were considered free. A lateral “incursion” of a previously immersed indenter on the crystallite from one of its ends was modeled as denoted in the scheme. The interaction between Ti atoms was described by a potential [41] constructed using the embedded atom method. A potential obtained within the frame of the modified embedded atom method was used to describe the interaction between titanium and vanadium atoms [42]. The model sample was considered as an NVT ensemble that maintains the number of atoms N , occupied volume V and the temperature of system T . All MD calculations were implemented using the LAMMPS [43]. To analyze the structure of the samples, the Dislocation Extraction Algorithm (DXA) and Common Neighbor Analysis (CNA) algorithms implemented in the open visualization tool OVITO were used [44].

4. RESULTS AND DISCUSSION

4.1 Experimental investigation of the scratching behavior of the EBAM Ti-6Al-4V samples

Typical microstructures observed in the EBAM Ti-6Al-4V samples are shown in Fig. 2. It is seen that the as-built sample exhibits a fine acicular α' -martensite lath structure within prior large-body primary β -grains (Fig. 2a). The thickness of the laths is 2-3 μm . The CEBS treatment resulted in increasing the thickness of the laths up to 5-7 μm and their fragmentation (Fig. 2b).

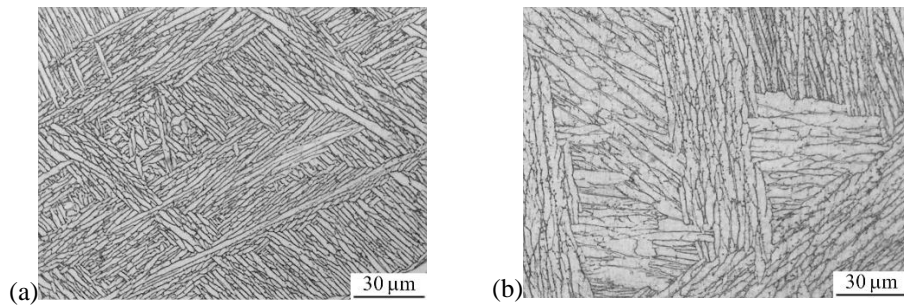


Fig. 2 Typical microstructures of (a) the as-built and (b) CEBS treated EBAM Ti-6Al-4V samples

The XRD patterns of the samples are illustrated in Fig. 3. The XRD pattern of the as-built sample shows the presence of only α -Ti peaks with a strong (100) texture. The CEBS treated EBAM Ti-6Al-4V sample also primarily demonstrates peaks of the α -Ti phase in the XRD pattern, but (100) preferred orientation became slightly less pronounced. In addition, the (110) peak of the β -Ti phase appears in the XRD pattern, which indicates the β -phase retained in the sample after its electron beam irradiation. An analysis of the results revealed that the volume fraction of β -Ti phase in the CEBS treated sample was 6.7 %.

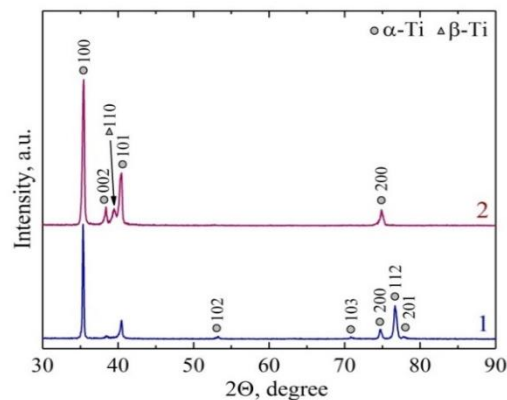


Fig. 3 X-ray diffraction patterns of (1) the as-built and (2) CEBS treated Ti-6Al-4V samples

The hardness and Young's modulus of the EBAM Ti-6Al-4V samples are listed in Table 1. It is seen that both samples are characterized by similar values of hardness and Young's modulus within experimental error. The H/E ratio of the sample subjected to post-manufacturing CEBS treatment, which is usually used to rank ductility and toughness of materials, is about 10% higher than that of the as-built sample.

Table 1. Mechanical properties of the EBAM Ti-6Al-4V samples.

Sample	H , GPa	E , GPa	H/E
1	3.91 ± 0.41	130 ± 4	0.030
2	4.22 ± 0.18	125 ± 6	0.034

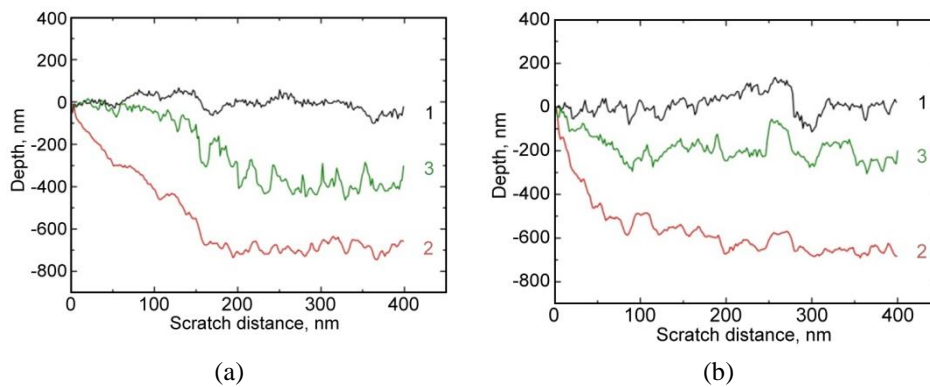


Fig. 4 Longitudinal surface profiles of scratch grooves in (a) the as-built and (b) CEBS treated EBAM Ti-6Al-4V samples: 1 – initial surface profile, 2 – residual scratch profile, 3 – scratch profile at the applied load

Fig. 4 displays longitudinal surface profiles scanned along scratch lines in the EBAM Ti-6Al-4V samples before, during and after scratching. It is seen that the CEBS treated sample is characterized by the smaller indenter penetration depth (~ 600 nm) and residual scratch depth (~ 250 nm) compared with the as-built sample (~ 700 and ~ 400 nm, correspondingly). This well agrees with the results of the AFM-investigations presented in Fig. 5. The AFM-images and cross-sectional surface profiles of the scratch grooves indicate that the scratching of the Ti-6Al-4V samples resulted in their ductile ploughing, which led to the formation of pile-ups along the groove flanks. Plastic ploughing of the material in the as-built sample resulted in the formation of symmetrical pile-ups along both edges of the track, whereas in the CEBS treated sample the pile-up was primarily formed only along one scratch flank. This is attributed to different crystallographic orientations of Ti crystallites subjected to plastic deformation in these samples with respect to the surface and the scratching direction, which favor activation of different slip systems [25, 40]. It is clearly seen in Fig. 5 that the as-built sample demonstrates wider and deeper residual scratch groove than the CEBS treated sample. According to the AFM results, the average depth and width of the scratch grooves are 405 ± 19 nm and 6.0 ± 0.1 μm , respectively, in the

as-built sample, while they decrease to 244 ± 17 nm and 3.1 ± 0.1 μm , respectively, in the CEBS treated sample.

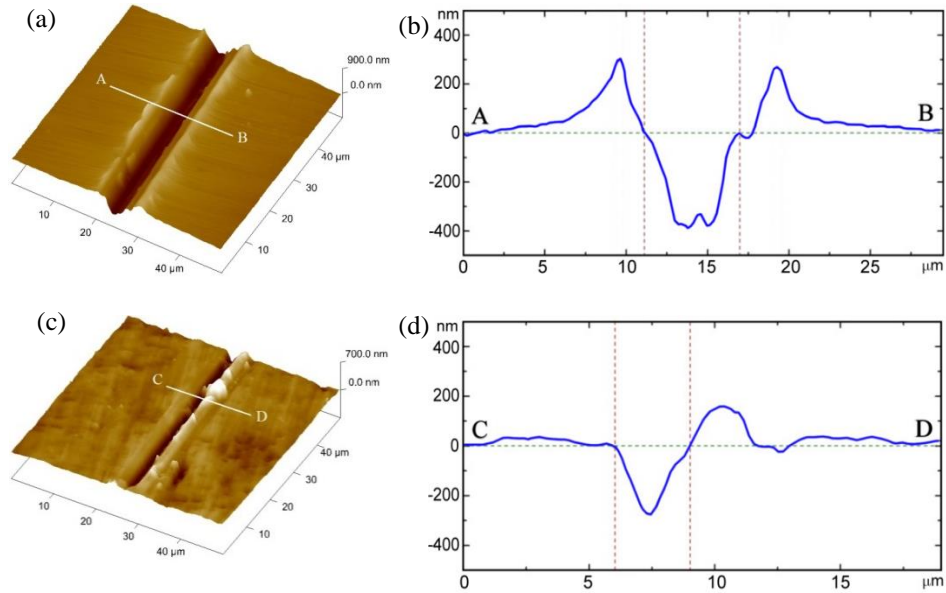


Fig. 5 AFM-images (a, c) and corresponding cross-sectional surface profiles (b, d) of scratch grooves formed at the applied load 200 mN in (a, b) the as-built and (c, d) CEBS treated EBAM Ti-6Al-4V samples.

4.2. MD simulation of scratching HCP and BCC Ti crystallites

Fig. 6 displays longitudinal profiles of the scratch grooves in the HCP and BCC Ti crystallites at different points of loading, when the indenter passed a distance of 10.7 nm (1, shown black), 18.2 nm (2, shown red) and 24.5 nm (3, shown blue). It is seen in Fig. 6 that the scratch depths under loading are the same at different time points and correspond to the penetration depth of the indenter into the sample (~ 3.5 nm). However, after unloading, i.e. moving the indenter away from the considered point, there is a difference in the recovery of the scratch grooves. The residual scratch depth in the BCC Ti crystallite (2.3-2.9 nm) is smaller than in the HCP crystallite (2.8-3.3 nm). This is even more clearly evidenced in Fig. 7, which exhibits cross-sectional surface profiles of scratch grooves in the Ti crystallites cut at $X = 10.7$ nm before, during and after loading. Substantially more pronounced recovery of the scratch groove is observed in the BCC crystallite compared with the HCP one. Thus, the results of the MD simulations well agree with the experimental findings.

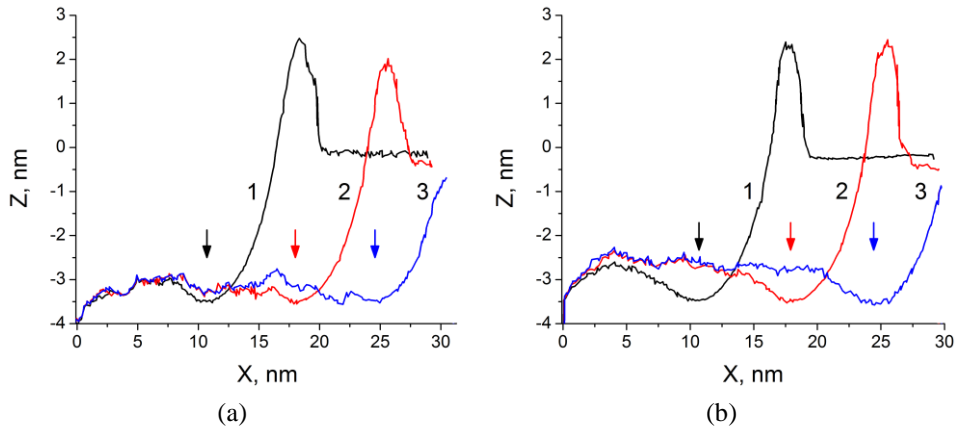


Fig. 6 Longitudinal surface profiles of scratch grooves in (a) HCP and (b) BCC Ti crystallites after different scratching distances: 1 – 10.7 nm, 2 – 18.2 nm, 3 – 24.5 nm. Arrows indicate the position of the indenter center at the corresponding time points

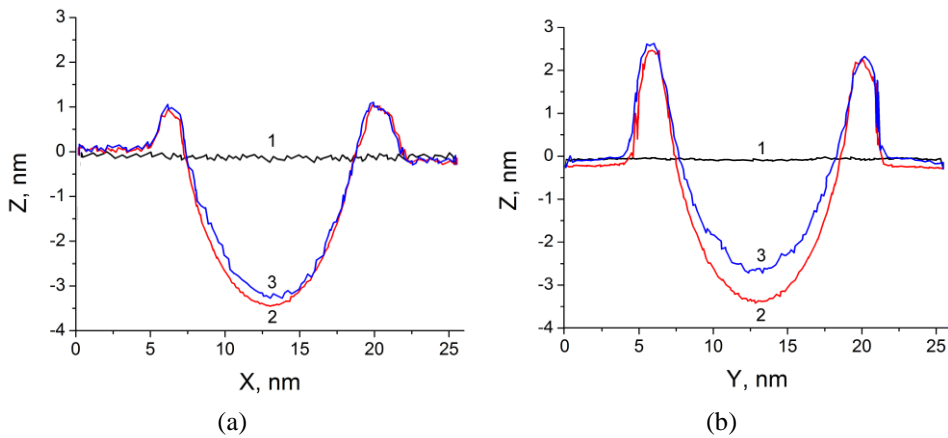


Fig. 7 Cross-sectional surface profiles of scratch grooves in (a) HCP and (b) BCC Ti crystallites cut at $X = 10.7$ nm at different points of loading: 1 – before loading, 2 – under loading (scratching distance is 10.7 nm), 3 – after unloading (scratching distance is 18.2 nm)

In order to gain insight into the physical mechanisms underlying the stronger recovery of the scratch grooves in the BCC titanium, the evolution of local atomic configurations during scratching the Ti crystallites was analyzed. The number of atoms belonging to HCP and BCC arrangement was plotted as a function of scratching distance for both Ti crystallites in Fig. 8. It can be seen that the crystallites demonstrate a decrease in the number of atoms belonging to the main matrix (HCP for crystallite 1 and BCC for crystallite 2) and an increase in the number of atoms with different local ordering (BCC for crystallite 1 and HCP for

crystallite 2) with increasing scratching distance. The first trend is attributed to continuously increasing the relative volume of the crystallites involved in plastic deformation, which results in disordering and fragmentation of their crystal structure. The second trend indicates the deformation-induced phase transformations HCP→BCC in crystallite 1 and BCC→HCP in crystallite 2), which occurred under loading. It should be noted that the number of BCC atoms in crystallite 1 increases until the end of scratching, whereas the number of HCP atoms in the crystallite 2 reaches the maximum value after ~9 nm of scratching, i.e. when the indenter passed approximately a third of the sample length, and nearly twice drops thereafter. The latter indicates that after unloading the HCP atoms in crystallite 2 can rearrange into the BCC structure, i.e. the reversible $\beta \leftrightarrow \alpha$ phase transformations can occur in β -Ti during scratching.

Figs. 9a-9c demonstrate evolution of the atomic structure of a fragment of the BCC titanium crystallite during scratching. In order to visualize atoms belonging to different types of the crystal lattice a CNA analysis was used. The comparison of Figs. 9a and 9b indicates that atomic rearrangement from the BCC lattice into the HCP local configuration occurs under compression induced by the indenter action. In addition, the formation of disordered atomic clusters is observed, which atomic configuration cannot be identified using CNA. When the indenter passed through the fragment, the majority of the HCP atoms rearranged again into the BCC lattice (Fig. 9c).

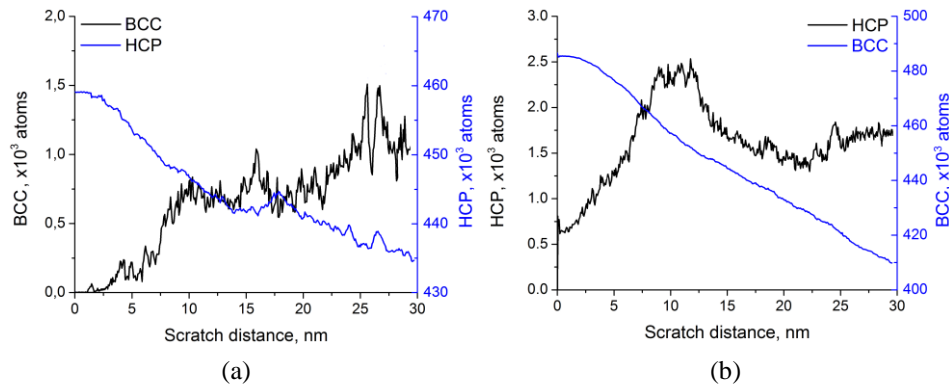


Fig. 8 Number of atoms belonging to HCP and BCC crystal lattice in (a) HCP and (b) BCC Ti crystallites as a function of scratching distance. Atoms with non-identified type of ordering are not shown

The possibility of the reversible $\beta \leftrightarrow \alpha$ phase transformations in vanadium-alloyed titanium is confirmed by the analysis of the total energy per atom performed using MD calculations for Ti crystallites. Fig. 10 shows the total energy per atom as a function of atomic volume in HCP and BCC Ti crystallites containing 13 at. % of vanadium, which is typical for the β -phase in Ti-6Al-4V alloy. It is seen that BCC configuration is energetically more favorable in equilibrium state before loading. However, the HCP structure becomes preferable at decreasing the volume per atom, i.e. under compression. Therefore, the transformation of β -Ti phase characterized by lower packing density into the more close-packed α -Ti phase can occur in the zones of compression beneath and ahead of the moving indenter. When the indenter moves away it results in the development of tensile stresses

behind it. Therefore, according to Fig. 10, the BCC arrangement becomes more favorable again that furthers the development of the reverse $\alpha \rightarrow \beta$ phase transformation. The reverse phase transformation results in the decrease in the number of the HCP atoms in the vanadium-alloyed Ti crystallite that explains its drop in Fig. 8b.

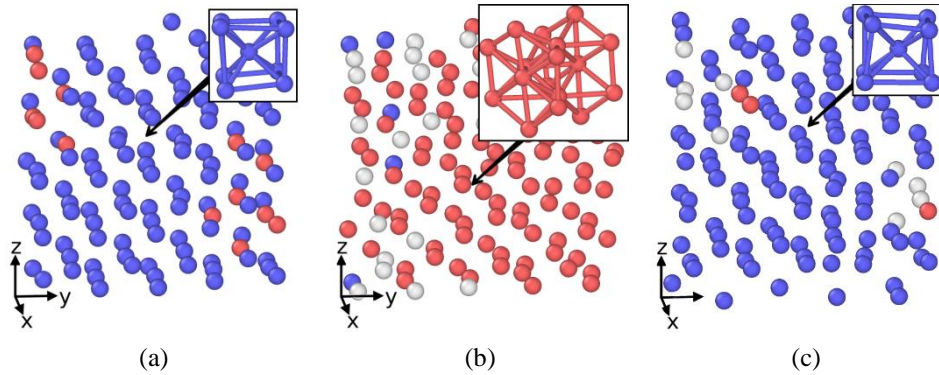


Fig. 9 Evolution of the atomic structure of the fragment of BCC Ti crystallite during scratching: a – before loading; b – under compression induced by indenter; c – after unloading. BCC atoms are shown blue, HCP atoms are shown red, and atoms belonging to unidentified local configurations are shown grey

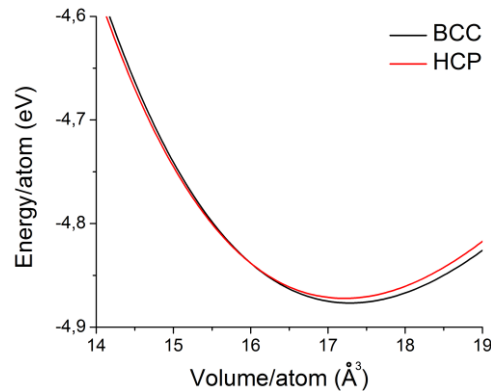


Fig. 10 Energy per atom in HCP and BCC Ti crystallites with 13 at. % of vanadium as a function of atomic volume

Evidently, the reversible $\beta \rightarrow \alpha \rightarrow \beta$ phase transformations can shed light on the origin of the experimentally observed enhanced recovery of the scratch groove in the CEBS treated EBAM Ti–6Al–4V sample. Since the as-built Ti–6Al–4V sample did not contain the β phase, the scratch recovery was only happened by means of relaxation of elastic strains. In contrast, the CEBS treated EBAM Ti–6Al–4V sample contained the β phase, so that the reversible $\beta \rightarrow \alpha \rightarrow \beta$ phase transformations could contribute to the densification of the material under loading and its additional recovery after unloading.

4. CONCLUSION

The microstructure, mechanical properties and scratching behavior of as-built EBAM Ti-6Al-4V samples and the samples subjected to post-manufacturing continuous electron beam scanning were investigated. The comparative study revealed that the CEBS post-treatment resulted in the transformation of the single phase α' -martensitic structure into the dual phase $\alpha+\beta$ structure. The microstructure evolution was accompanied by increasing the ratio of hardness to Young's modulus, which indicated the improvement of toughness and ductility of the CEBS treated Ti-6Al-4V. Scratch testing of the samples revealed significant improvement of deformation recovery of scratch grooves in the CEBS treated EBAM Ti-6Al-4V sample compared with the as-built sample. Molecular dynamics simulation of scratching Ti crystallites with HCP and BCC structure was performed to gain insight into the physical origins of the enhanced deformation recovery. The simulation showed that reversible $\beta\rightarrow\alpha\rightarrow\beta$ phase transformations can be one of the mechanisms responsible for the experimentally observed enhanced recovery of the scratch groove in the CEBS treated EBAM Ti-6Al-4V samples containing β phase. These phase transformations can occur in the vanadium alloyed BCC Ti crystallites in the zones of compression beneath and ahead the moving indenter, because the more closed packed α -Ti phase becomes more energetically favorable. Thus, the study showed the possibility to use the post-manufacturing CEBS process to improve the microstructure and mechanical properties of EBAM Ti-6Al-4V alloy.

Acknowledgements: *The research was performed according to the Government research assignment for ISPMS SB RAS, projects FWRW-2021-0006 and FWRW-2021-0010, and was funded by RFBR and Tomsk region, project number 18-48-700009.*

REFERENCES

1. Froes, F.H., 2015, *Titanium: Physical Metallurgy, Processing and Application*, ASM International: Materials Park, OH, USA.
2. Bermingham, M.J., Kent, D., Zhan, H., StJohn, D.H., Dargusch, M.S. 2015, *Controlling the microstructure and properties of wire arc additive manufactured Ti-6Al-4V with trace boron additions*, Acta Materialia, 91, pp. 289-303.
3. Dutta, B., Froes, F.H., 2015, *The Additive Manufacturing (AM) of titanium alloys*, In: Qian, M., Froes, F.H. (Eds.), *Titanium Powder Metallurgy*, Elsevier, Ed., Butterworth-Heinemann, Oxford, UK, pp. 447-468.
4. Gorsse, S., Hutchinson, C., Gouné, M., Banerjee R. 2017, *Additive manufacturing of metals: a brief review of the characteristic microstructures and properties of steels, Ti-6Al-4V and high-entropy alloys*, Science and Technology of Advanced Materials, 18(1), pp. 584-610.
5. Liu, S., Shin, Y.C. 2019, *Additive manufacturing of Ti6Al4V alloy: A review*, Materials & Design, 164, 107552.
6. Lin, Z., Song, K., Yu, X., 2021, *A review on wire and arc additive manufacturing of titanium alloy*, Journal of Manufacturing Processes, 70, pp. 24-45.
7. Herzog, D., Seyda, V., Wycisk, E., Emmelmann, C., 2016, *Additive manufacturing of metals*, Acta Materialia, 117, pp. 371-392.
8. Wang, X., Chou, K., 2018, *EBSD study of beam speed effects on Ti-6Al-4V alloy by powder bed electron beam additive manufacturing*, Journal of Alloys and Compounds, 748, pp. 236-244.
9. Dumontet, N., Connétable, D., Malard, B., Viguier, B., 2019, *Elastic properties of the α' martensitic phase in the Ti-6Al-4V alloy obtained by additive manufacturing*, Scripta Materialia, 167, pp. 115-119.
10. Rafi, H.K., Karthik, N.V., Gong, H., Starr, T.L., Stucker, B.E., 2013, *Microstructures and mechanical properties of Ti6Al4V parts fabricated by selective laser melting and electron beam melting*, Journal of Materials Engineering and Performance, 22, pp. 3873-3883.
11. Xu, W., Lui, E.W., Pateras, A., Qian, M., Brandt, M., 2017, *In situ tailoring microstructure in additively manufactured Ti-6Al-4V for superior mechanical performance*, Acta Materialia, 125, pp. 390-400.

12. Wycisk, E., Siddique, S., Herzog, D., Walther, F., Emmelmann, C., 2015, *Fatigue performance of laser additive manufactured Ti-6Al-4V in very high cycle fatigue regime up to 10^9 cycles*, *Frontiers in Materials*, 2, 72.
13. Wu, S.Q., Gan, Y.L., Huang, T.T., 2016, *Microstructural evolution and microhardness of a selective-laser-melted Ti-6Al-4V alloy after post heat treatments*, *Journal of Alloys and Compounds*, 672, pp. 643-652.
14. Nicoletto, G., Maisano, S., Antolotti, M., 2017, *Influence of post fabrication heat treatments on the fatigue behavior of Ti-6Al-4V produced by selective laser melting*, *Procedia Structural Integrity*, 7, pp. 133-140.
15. DebRoy, T., Wei, H.C., Zuback, J.S., Mukherjee, A.M., Elmer, J.W., Milewski, J.O., Beese, A.M., Wilson-Heid, A., De, A., Zhang, W., 2018, *Additive manufacturing of metallic components – Process, structure, properties*, *Progress in Materials Science*, 92, pp. 112-224.
16. Raghaven, S., Nai, M.L.S., Wang, P., Sin, W.J., Wei, J., Li, T., 2018, *Heat treatment of electron beam melted (EBM) Ti-6Al-4V: microstructure to mechanical property correlations*, *Rapid Prototyping Journal*, 24(4), pp. 774-783.
17. Sayed, A.K., Awd, M., Walther, F., Zhang, X., 2019, *Microstructure and mechanical properties of as-built and heat-treated electron beam melted Ti-6Al-4V*, *Materials Science and Technology*, 35(6), pp. 653-660.
18. Abu-Issa, A., Lopez, M., Pickett, C., Escarcega, A., Arrieta, E., Murr, L.E., Wicker, R.B., Ahlfors, M., Godfrey, D., Medina, F., 2020, *Effects of altered hot isostatic pressing treatments on the microstructures and mechanical performance of electron beam melted Ti-6Al-4V*, *Journal of Materials Research and Technology*, 9(4), pp. 8735-8743.
19. Rotshtein, V.P., Proskurovsky, D.I., Ozur, G.E., Ivanov, Y.F., Markov, A.B., 2004, *Surface modification and alloying of metallic materials with low-energy high-current electron beams*, *Surface and Coatings Technology*, 180-181, pp. 377-381.
20. Walker, J.C., Murray, J.W., Nie, M., Cook, R.B., Clare, A.T., 2014, *The effect of large-area pulsed electron beam melting on the corrosion and microstructure of a Ti6Al4V alloy*, *Applied Surface Science*, 311, pp. 534-540.
21. Shinonaga, T., Yamaguchi, A., Okamoto, Y., Okada, A., 2021, *Surface smoothing and repairing of additively manufactured metal products by large-area electron beam irradiation*, *CIRP Annals*, 70, pp. 143-146.
22. Panin, A., Kazachenok, M., Perevalova, O., Martynov, S., Panina, A., Sklyarova, E., 2019, *Continuous electron beam post-treatment of EBF³-fabricated Ti-6Al-4V parts*, *Metals*, 9, 699.
23. Kim, J., Kim, J.S., Kang, E.G., Park, H.W., 2014, *Surface modification of the metal plates using continuous electron beam process (CEBP)*, *Applied Surface Science*, 311, pp. 201-207.
24. Li, W., Ma, R., Chen, D., Yao, Z., Song, K., Yu, L., Wang, Z., Li, Y., Liao, J., 2021, *The effect of continuous electron beam scanning process on the microstructure and geometry of U-5.5 wt%Nb alloy*, *Nuclear Instruments and Methods in Physics Research Section B*, 496, pp. 16-28.
25. Shugurov, A.R., Panin, A.V., Dmitriev, A.I., Nikonov, A.Yu., 2018, *The effect of crystallographic grain orientation of polycrystalline Ti on ploughing under scratch testing*, *Wear*, 408-409, pp. 214-221.
26. Kimm, J., Sander, M., Pöhl, F., Theisen, W., 2019, *Micromechanical characterization of hard phases by means of instrumented indentation and scratch testing*, *Mater. Sci. Eng. A*, 768, 138480.
27. Machado, P.C., Pereira, J.I., Penagos, J.J., Yonamine, T., Sinatora, A., 2017, *The effect of in-service work hardening and crystallographic orientation on the micro-scratch wear of Hadfield steel*, *Wear*, 376-377, pp. 1064-1073.
28. Dmitriev, A.I., Nikonov, A.Y., Shugurov, A.R., Panin, A.V., 2019, *The role of grain boundaries in rotational deformation in polycrystalline titanium under scratch testing*, *Physical Mesomechanics*, 22, pp. 365-374.
29. Liu, J., Zeng, Q., Xu, S., 2020, *The state-of-art in characterizing the micro/nano-structure and mechanical properties of cement-based materials via scratch test*, *Constr. Build. Mater.*, 254, 119255.
30. Chavoshi, S.Z., Gallo, S.C., Dong, H., Luo, X., 2017, *High temperature nanoscratching of single crystal silicon under reduced oxygen condition*, *Mater. Sci. Eng. A*, 684, pp. 385-393.
31. Wang, B., Melkote, S.N., Saraogi, S., Wang, P., 2020, *Effect of scratching speed on phase transformations in high-speed scratching of monocrystalline silicon*, *Mater. Sci. Eng. A*, 772, 138836.
32. Zhang, P., Zhao, H., Shi, C., Zhang, L., Huang, H., Ren, L., 2013, *Influence of double-tip scratch and single-tip scratch on nano-scratching process via molecular dynamics simulation*, *Appl. Surf. Sci.*, 280, pp. 751-756.
33. Zhu, P., Hu, Y., Fang, F., Wang, H., 2012, *Multiscale simulations of nanoindentation and nanoscratch of single crystal copper*, *Appl. Surf. Sci.*, 258, pp. 4624-4631.
34. Ren, J., Hao, M., Lv, M., Wang, S., Zhu, B., 2018, *Molecular dynamics research on ultra-high-speed grinding mechanism of monocrystalline nickel*, *Appl. Surf. Sci.*, 455, pp. 629-634.

35. Gao, Y., Ruestes, C.J., Urbassek, H.M., 2014, *Nanoindentation and nanoscratching of iron: Atomistic simulation of dislocation generation and reactions*, *Comput. Mater. Sci.*, 90, pp. 232–240.
36. Wu, C.-D., Fang, T.-H., Lin J.-F. 2012, *Atomic-scale simulations of material behaviors and tribology properties for FCC and BCC metal films*, *Mater. Lett.*, 80, pp. 59–62.
37. Alhafez, I.A., Urbassek, H.M. 2016, *Scratching of hcp metals: A molecular-dynamics study*, *Computational Material Science*, 113, pp. 187-197.
38. American Society for Testing and Materials, 2013, *ASTM B348-13, Standard specification for titanium and titanium alloy bars and billets*, ASTM International, West Conshohocken, PA.
39. Oliver, W.C., Pharr, G.M., 1992, *An improved technique for determining hardness and elastic modulus using load and displacement sensing indentation experiments*, *Journal of Materials Research*, 7(6), pp. 1564-1583.
40. Dmitriev, A.I., Nikonov, A.Y., Shugurov, A.R., Panin, A.V., 2019, *Numerical study of atomic scale deformation mechanisms of Ti grains with different crystallographic orientation subjected to scratch testing*, *Applied Surface Science*, 471, pp. 318-327.
41. Mendeleev, M.I., Underwood, T.L., Ackland, G.J., 2016, *Development of an interatomic potential for the simulation of defects, plasticity, and phase transformations in titanium*, *Journal of Chemical Physics*, 145, 154102.
42. Maisel, S.B., Ko, W.-S., Zhang, J.-L., Grabowski, B., Neugebauer, J., 2017, *Thermomechanical response of NiTi shape-memory nanoprecipitates in TiV alloys*, *Physical Review Materials*, 1, 033610.
43. Plimpton, S., 1995, *Fast parallel algorithms for short-range molecular dynamics*, *Journal of Computational Physics*, 117(1), pp. 1-19.
44. Stukowski, A., Bulatov, V.V., Arsenlis, A., 2012, *Automated identification and indexing of dislocations in crystal interfaces*, *Modeling and Simulation in Materials Science and Engineering*, 20, 085007.